Performance, radiation shielding, and anti-fungal activity of alkali-activated slag individually modified with zinc oxide and zinc ferrite nano-particles

Alaa Mohsen [a], Hamdy A. Abdel-Gawwad [b,*], M. Ramadan [c]

[a] *Faculty of Engineering, Ain Shams University, Cairo, Egypt*
[b] *Raw Materials and Processing Technology Research Institute, Housing and Building National Research Center, Cairo, Egypt*
[c] *Chemistry Department, Faculty of Science, Ain Shams University, Cairo, Egypt*

HIGHLIGHTS

- Nano zinc oxide (NZO) and -zinc ferrite (NZF) were prepared in this study.
- Adding NZO retards the early-hydration rate of alkali-activated slag (AAS).
- Embedding NZF in activated system causes the improvement of early-AAS properties.
- The mixture having 1.5 wt% NZF demonstrates the highest mechanical properties.
- Nano-modified-AAS showed the highest radiation shielding and anti-bacterial action.

ARTICLE INFO

ABSTRACT

In this paper, low-cost nano-zinc ferrite (NZF) was used to evaluate its efficacy, as compared with nano-zinc oxide (NZO), on the performance of the fresh and hardened alkali activated slag (AAS). An elongation in setting times and a reduction in early-ages' compressive strengths were recorded in the case of AAS individually containing 0.5, 1, and 1.5 wt% NZO. A turning point was observed after 3 days of curing as AAS-NZO set represents compressive strengths higher than those of reference sample. The embedding NZF in alkali activated system has resulted in setting time shortening and mechanical properties improvement at both early and later ages. This means that the acceleration effect of nano-ferrite compensates the retardation impact of NZO on the activation of AAS-hydration. Regardless its promising properties, AAS-NZF composites demonstrate compressive strength, γ-ray radiation shielding, and anti-fungal activity higher than those recorded in the case of AAS-NZO one at all addition levels.

1. Introduction

Nowadays, the population explosion is considered as one of the biggest challenges that facing the world as it is causing a dramatic consumption in natural resources. Urban expansion is the other side resulting from the process of population increment, which in turn led to the expansion of some industries that have a harmful impact on the environment such as cement industry [1,2]. As one of the eco-friendly cements, alkali activated slag (AAS) was used as a good alternative to Portland cement (PC) in the most if not all construction applications [3–5]. AAS was discovered by Purdon [6], which stated that the mixing of alkaline solution with blast fur-nace slag (BFS) followed by curing (at ambient temperature) has resulted in the formation hardened materials with high mechanical and durable properties. Nevertheless, high shrinkage [7,8], quick setting [9] and low flowability are the main limiting issues to the use of AAS. These drawbacks play a big role in the non-acceptance of AAS as construction materials.

Most recent researches are focused on how to expand the use of AAS in many applications; therefore they are always interested in improving their mechanical and physico-chemical properties. In such cases, nanoparticles can be added to AAS matrix composite, for enhancing its performance to be beneficially used in different applications. Nanotechnology is considering one of the most important fields which used to develop new materials with high performance. This positive effect is mainly originated from the high surface area of nano-materials which reflects on their high

reactivity. Nano-SiO_2 [10,11], nano-Al_2O_3 [12] and nano-ZnO [13] are the most nano materials which were used to enhance the performance of AAS including compressive and flexural strengths and the dry shrinkage reduction. Additionally, they improve the AAS-durability in chloride- and sulphate-rich-media.

One of the most annoying things facing ancient underground AAS structures is the detrimental impact caused by microbial activity [14]. The detrimental impact of biological activity is caused by the formation of microbial biofilm on the AAS-surface, leading to chemical damage and cracking accompanied by a dramatic regression in its mechanical properties. Specifically, the attack of SOB with AAS has resulted in a dramatic regression in its mechanical properties which mainly caused by the biogenic sulfuric acid produced by this bacterial strain [15]. Therefore, many techniques were developed to mitigate the detrimental impact of microbial attack on the performance AAS. Recently nano-materials-containing-heavy metals such as Fe, Mn, Mo, Zn, Co, V and Cr were prepared to be used as antimicrobial. Heavy metal ions (M^+) form a complex compound when react with negatively charged membrane of microbial cell causes an inhibition in enzymatic microbial activity [16]. In the recent published work by Abdel-Gawwad et al [17], the utilization of lead-bearing-sludge as a substituent to slag not only mainly contributed to the enhancement of AAS-performance but it was also strongly improved its resistivity to different bacterial and fungal species. ZnO nanoparticles is considered one of the most important semiconductors that used widely in various applications such as photocatalytic degradation of dangerous pollutants and antimicrobial activity [18,19]; these acquired properties is attributed to high oxidizing power of NZO under solar irradiation which help to generate reactive oxygen species that inhibit the microbial growth [20,21]. The bacterial and fungal resistivity was enhanced for some cementitious composites modified with 5–15% commercial ZnO nanoneedles [22]. The antibacterial activity of ZnO and Ag NPs for cement mortar against the growth of gram positive Bacillus cereus and gram negative Escherichia coli had been affirmed by Noeiaghaei et al 2017 [23]. The fly-ash based geopolymer incorporated with 6% ZnO-SiO_2 nanohybride exhibited high strength with anti-microbial efficiency [14]. The inclusion of 2% ZnO-whiskers (tetra-needle crystals) has reinforced the flexural, tensile and compressive strengths of OWC pastes [24]. Unfortunately, ZnO nanoparticles had demonstrated strong negative returns on the strength of all cementitious materials in the early ages (1–3 days) of hydration due to the retardation phenomenon of the generated $Zn(OH)_2$ barrier layers [25–27].

Though the nuclear technology is introduced in many important applications as in medicine, industry and agriculture, the radiations emissions (X-, β-, γ-rays and neutrons) have a harmful impact on the human health and environment. Therefore, there is a great need to develop materials with high shielding property to nuclear-radiations [28]. Recently, hematite (α-Fe_2O_3) and spinel ferrites NPs play a vital role in the improvement of the mechanical characteristics of cementitious composites particular in the early ages of hydration as well as upgrade the shielding property against harmful radiations. Abo-El-Enein et al affirmed that the attenuation coefficient of OPC increased by 11% in presence of 2% α-Fe_2O_3 NPs [29]. Spinel ferrites NPs with specific crystallographic structure (tetrahedral/octahedral geometry) such as $ZnFe_2O_4$, $MgFe_2O_4$, $NiFe_2O_4$, Fe_3O_4 and $CoFe_2O_4$ [30,31] were utilized in recent publications for shielding applications. They acted as dosimetric materials with high absorption power for harmful radiations [32]. The inclusion of 1% $MgFe_2O_4$ or 1% $ZnFe_2O_4$ NPs could improve, after 28-days of hydration, the attenuation coefficient values of cementitious composites by 32% and 26% respectively [33,34]. Among all spinel, $ZnFe_2O_4$ NPs was used in various applications as antimicrobial agent [31,35] but up to our knowledge this spinel has not been used before as a chemical admixture in cemen-

titious matrices with synergetic effects that combine between the antimicrobial activity and radiation shielding with enhancing the mechanical properties at all ages of hydration.

In this framework, present effort is designed to make modification on nano-ZnO particles, to be useful for different applications without affecting on the AAS strength. Nano hybrids-$ZnFe_2O_4$ was prepared from commercial materials, to maximize the benefits of nano-ZnO and nano-Fe_2O_3 together. Comparison between addition of nano-ZnO and nano-hybrids-$ZnFe_2O_4$ was addressed, to evaluate the effect of nano particles composites on the properties of AAS. The antimicrobial efficiency and radiation shielding of AAS containing these nano materials were examined to enhance the feasibility of utilizing nano-modified AAS in useful applications.

2. Experimental

2.1. Resources of materials and their characterizations

Ground granulated blast furnace slag (GGBFS) with Blaine fineness of 3950 Cm^2/g was supplied by Lafarge Company (Suez, Egypt). Sodium hydroxide (NaOH) with purity of 99.99% was obtained from EL-Gomhoria Chemical Company (Cairo, Egypt). Commercial zinc acetate dihydrate ($Zn(CH_3COO)_2·2H_2O$), ferric chloride hexahydrate ($FeCl_3·6H_2O$), ammonium hydroxide (28%, NH_4OH), and different types of surfactants chitosan and cetyl trimethyl ammonium bromide (CTAB) were purchased from Adwic El-Nasr Company (Qalyubia, Egypt). The complete chemical analysis, which was carried out by X-ray fluorescence (XRF: Xios, style PW-1400), of GGBFS was recorded in Table 1. A typical amorphous X-ray diffraction (XRD) pattern (Fig. 1) with a hump at 2θ° of 15–30 was observed in the case of GGBFS. The appearance of some weak crystalline peaks affiliated to gehlenite and akermanite is an indication of the main mineralogical compositions of GGBFS, complying with the previous published works [17].

2.2. Preparation of nano materials

Sol–gel technique was used to prepare nano-zinc oxide (NZO) and nano-zinc ferrite (NZF) spinel. The former was prepared by stirring 0.5 M $Zn(CH_3COO)_2·2H_2O$ in the presence of 2% (w/v) chitosan for an hour, followed by adjusting pH at 7 using NH_4OH. After that, the stirring process was completed for an hour again then left for 24 h. The precipitated gel was filtrated using filter paper (0.22 μm) and washed several times using distilled and deionized waters followed by drying at 80 °C overnight. The solid-

Table 1
. Chemical oxide compositions of GGBFS.

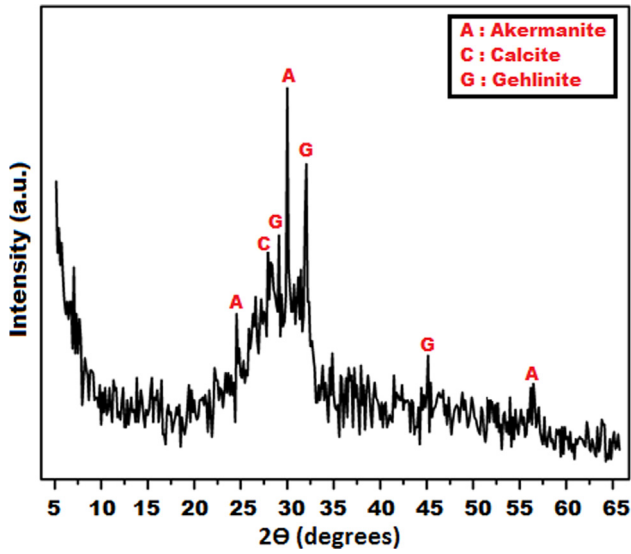| Oxides	Mass (%)
SiO_2	51
Al_2O_3	12.7
Fe_2O_3	0.3
CaO	25.4
MgO	7.25
SO_3	1.84
Na_2O	0.49
K_2O	0.18
TiO_2	0.3
MnO	0.06
BaO	0.04
P_2O_5	0.18
SrO	0.02
ZrO_2	0.01
Cl^-	0.04
L.O.I	0.1

Fig. 1. XRD-patterns of GGBFS.

ified material was gently grinded before calcination at 500 °C for 3 h [36,37]. The same steps were conducted to prepare NZF using 0.5 M $Zn(CH_3COO)_2 \cdot 2H_2O$ and 1 M $FeCl_3 \cdot 6H_2O$ solution in presence of 10% (w/v) CTAB dispersing agent at mentioned above calcination conditions [38–40].

Scanning electron microscope (SEM) (Fig. 2) shows that the prepared NZO has spherical shaped with particle size lower than that of NZF. This does not reflect the actual particle size of each; the agglomeration property of nanoparticles may cause a pseudo observation. Energy dispersive X-ray analyzer confirmed that the prepared NZO and NZF have purity of 100 and 99.1%, respectively. High resolution transmission electron microscopy (HR-TEM) (Fig. 3) was conducted to measure the actual particle size of the prepared nano-materials. It is perfectly proved that the prepared NZO demonstrates particle size ranging from 32 to 93 nm; whereas NZF recorded smaller particle size (15–25 nm). Complementary, the XRD-analysis proved the sol gel method has high efficiency to yield NZO and NZF with high purity as shown in Fig. 4. The complete adsorption/desorption isotherms of the prepared NPs (Fig. 5) confirms the higher NZF adsorption capacity (S_{BET} of 87.1 m^2/g) compared to that of NZO (S_{BET} of 11.4 m^2/g). Table 2 clarifies some important properties for the synthesized NPs.
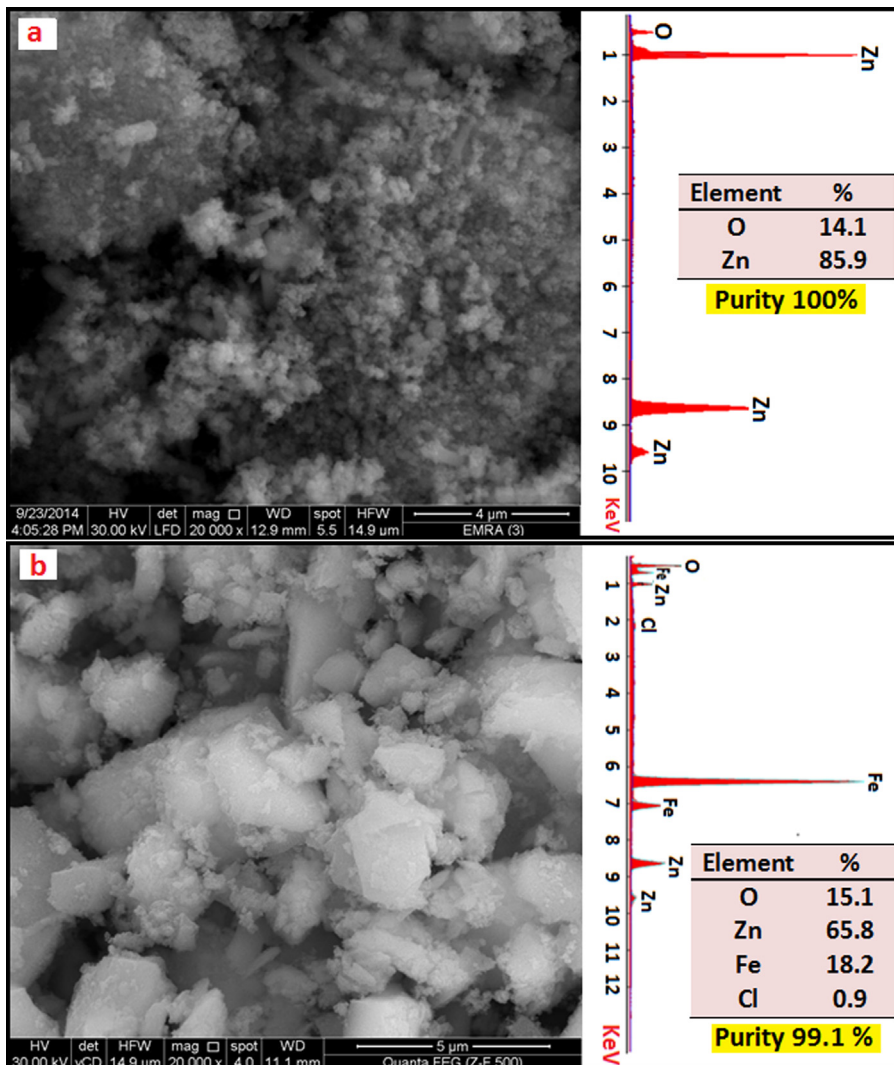

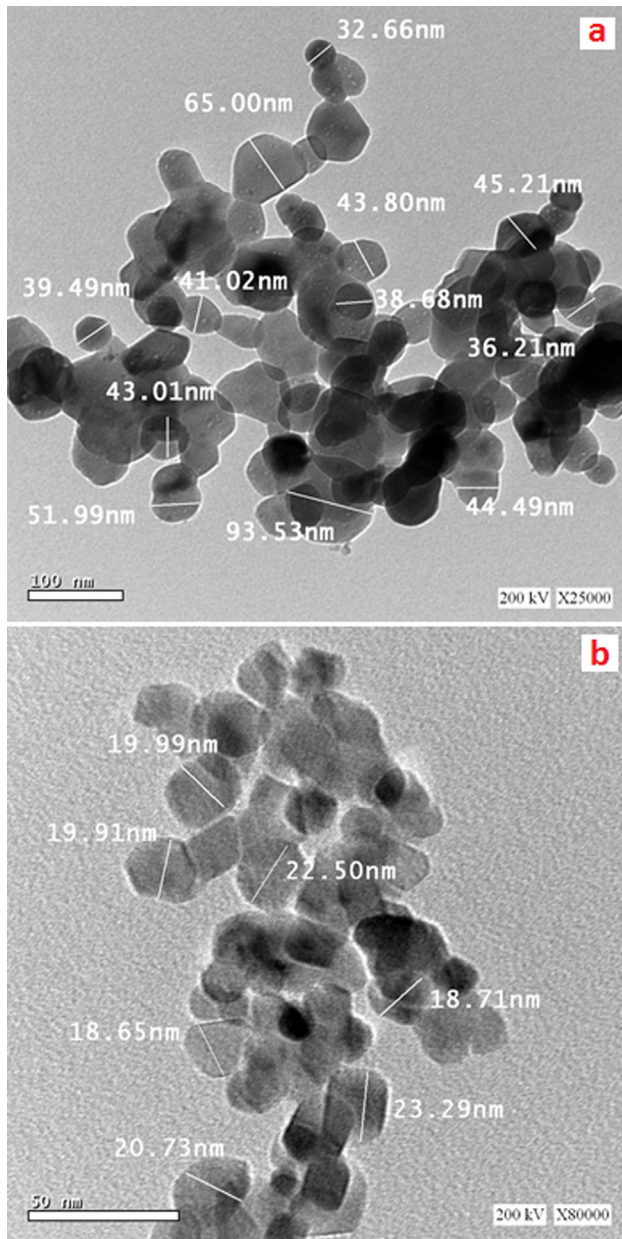
Fig. 2. SEM/EDX images for: (a) NZO and (b) NZF.

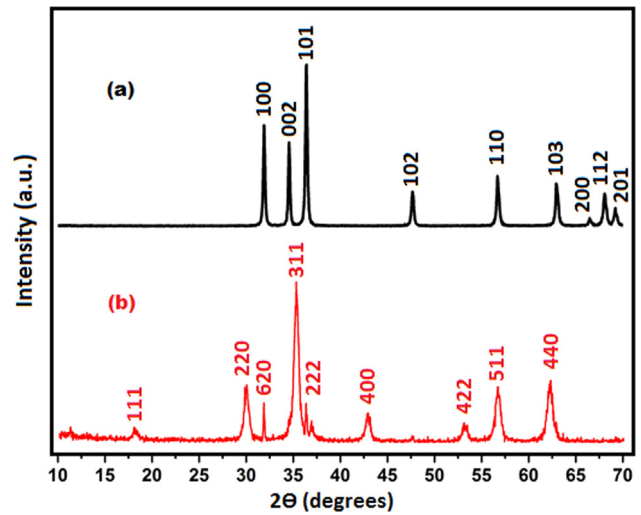**Fig. 3.** HRTEM images for: (a) NZO and (b) NZF.

Fig. 4. XRD-patterns for (a) NZO and (b) NZF.
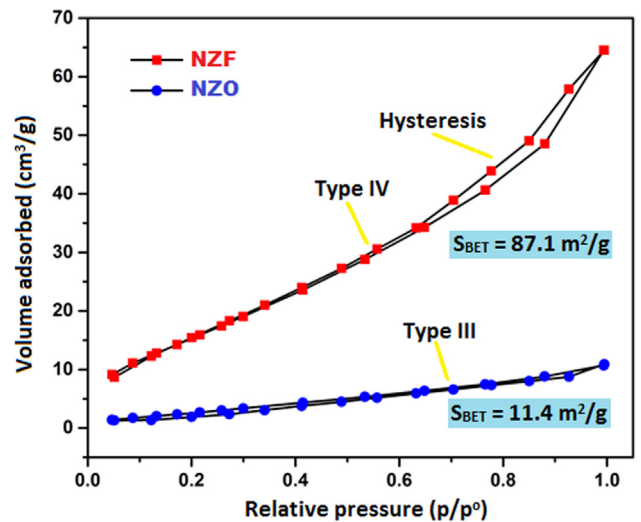

Fig. 5. N_2-adsorption/desorption isotherms for NZO and NZF.

Table 2
. General characteristics of NZO and NZF nanoparticles.

Property	Average particle size (nm)	S_{BET} (m^2/g)	Bulk Density (g/cm^3)	Refractive index	pH	Purity (%)
NZO	50 ±5	11.4	0.63	2.0021	9.1	100
NZF	20 ±5	87.1	2.56	1.9533	9.3	99.1

2.3. Preparation of alkali activated slag pastes and curing

Before preparation of fresh pastes, the NaOH-solution was prepared by dissolving 3% NaOH (respect to the powder weight) in water (equivalent to water / GGBFS ratio of 0.25), then kept for 24 h before its mixing with GGBFS to avoid the heat released during the dissolution of alkali. Low percentage of NaOH was used to reduce the environmental impact and cost of the prepared AAS [17]. The preparation of alkali activated slag (AAS) was conducted by mixing GGBFS-powder with NaOH solution to make workable pastes. For the mixtures individually containing NZO and NZF, the nano-materials was previously suspended in NaOH solution and sonicated for 15 min to ensure full dispersion of nano-particles. After mixing process by means of a good mixer and vibrating table, the homogeneous AAS-pastes were casted in 25 × 25 × 25 mm stainless steel mold, followed by curing in 99 ± 1% relative humidity (RH) at 23 ± 2 °C overnight. The hardened AAS-pastes were demolded and cured at the same

condition until testing times. The details of mix proportions are given in Table 3.

2.4. Experimental methods

According to standard ASTM C1611 [41], the workability represents the flow behavior of the freshly cement paste. Mini-slump mold with 60 mm in height, 20 mm in top diameter, and 40 mm in bottom diameter was used to determine the workability of the fresh AAS-paste. Typically, in the mini-slump test, a mould of a given conical shape from interior is filled with the material to be tested. The mould is then lifted and flow occurs. From a practical

Table 3
. Mix proportions of the prepared alkali activated composite (wt, %).

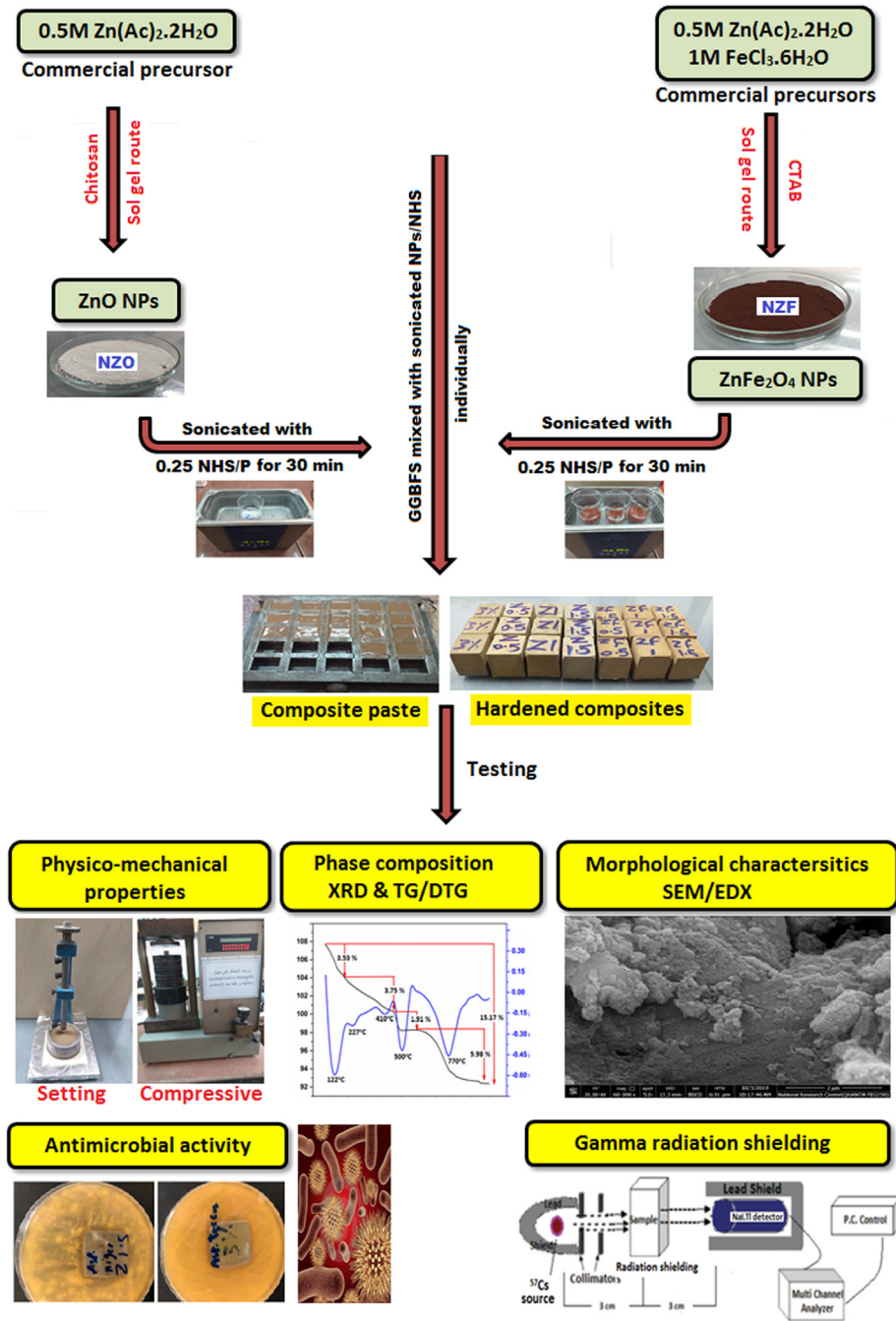| Sample notation	GGBFS	NZO	NZF	NaOH	W/GGBFS
AAS	100	–	–	3	0.25
AAS-NZO-0.5	100	0.5	–	3	0.25
AAS-NZO-1	100	1	–	3	0.25
AAS-NZO-1.5	100	1.5	–	3	0.25
AAS-NZF-0.5	100	–	0.5	3	0.25
AAS-NZF-1	100	–	1	3	0.25
AAS-NZF-1.5	100	–	1.5	3	0.25

Fig. 6. Schematic diagram for all of the experimental work.

point of view, the spread diameter is measured so we can determine the radius to calculate the spread area ($A = \pi r^2$). The paste of higher spread area is the highest in workability. The workability of the paste mainly depends on the paste compositions, surface areas of the components, water/ binder ratio and addition of some surfactants (super-plasticizers) [42]. The initial and final setting

times were examined using Vicat apparatus according to ASTM C191 [43]. The mechanical strength was conducted on three-cubes of the hardened AAS-pastes according to ASTM C109M [44] at each curing age using a Ton-Industrie instrument with a maximum loading capacity of 60 tons. After 28 days of hydration, total porosity (TP) % and bulk density (BD) were calculated according ASTM (C140) [45] as the following,

$$TP, \% = \frac{Wo - Wd}{Wo - Ws} * 100 \text{ and } BD = \frac{Wd}{Wo - Ws}$$

where: Wo, Ws and Wd are the weights of saturated, suspended and dried (at 100 °C overnight) sample, respectively.

2.5. Instrumental techniques

Fourier transform infrared (FTIR) spectroscopy (Genesis-II FT-IR spectrometer using KBr) was used to identify the functional groups in the hardened materials at wavenumber range of 400–4000 cm^{-1}. The chemical changes that occurred in hydration phases were detected using thermo gravimetric analysis/its derivative (TGA/DTG) (TA instrument style SDT Q600 heating rate of 20 °C/min in helium). XRD (Philips Xpert 2000, Holland) was carried out using a scanning range of 10 to 50 (2θ°), with a scanning speed of 1 s/step and resolution of 0.05°/step to study the binding phases composition. Also, SEM was used to investigate the morphology and micro-structure of hardened binding phases using Inspect S (FEI Company, Holland) equipped with an energy dispersive X-ray analyzer (EDXA).

2.6. Radiation shielding efficiency

The effect of nano materials on shielding efficiency of Gamma radiation was measured for hardened AAS-pastes with or without NZO and NZF. ^{57}Cs was used as a 0.662 MeV gamma source and NaI.Tl as detector. After 28 days of curing, intensity of transmitted gamma radiation was measured with varying the thickness by using four cubes for each mix. From Beer-Lambert law the linear attenuation coefficient (μ) was calculated [29,33].

2.7. Anti-microbial activity

The effect of the different types of fungal stains (*Aspergillums fumigatus ATCC 26933*, *Aspergillums niger ATCC 1015* and *Aspergillums terreus ATCC 20542*) on the control AAS sample and AAS individually containing 1.50 wt% NZO and NZF was evaluated. Initially hardened samples were cut in form of discs (2.5 cm length, 2.5 cm width and 0.3 cm thickness), then immersed in water to reduce the pH (≤ 8.0). The reason behind lowering pH is the avoiding the potential impact on microbial growth inhibition, ensuring that the nano-materials is the only reason for microbial inhibition [15,17,46].

The anti-fungal activity was assessed by placing 30 ml of Sabroud dextrose agar (SDA) medium, autoclaved at 121 °C and pressure 15 Ibs, in Petri dish. 0.1 ml of suspended fungal spores was used to solidify the SDA medium, followed by placed the hardened sample disc in the dish and incubated at 28 °C for 30 days. After that, fungal growth was measured according to ASTM D4300-1 [17,47]. Finally, Fig. 6 displays a block diagram to summarize all of the experimental work.

3. Results and discussion

3.1. Physical and mechanical properties

Generally, the spread area of the fresh AAS cement pastes is an indication of their workability. The wider the spread area is, the higher the workability is. As shown in Fig. 7(a, b), the addition of 0.5, wt. % NZO has no effect on the workability of alkali activated system. A marginal effect on flowability of AAS was recorded in the case of fresh pastes having 1 and 1.5 wt% NZO. NZF represents a stronger effect on the workability reduction as compared with NZO. Specifically, the addition of 0.5, 1, and 1.5 wt% NZF has resulted in the decrease of workability by ~ 5, 13, and 17%, respectively. The possible reason behind the negative impact of nano particles on workability of the fresh AAS-paste is caused by the high surface area of nano oxide, which requires higher water content to achieve the optimum workability. Moreover, the higher surface area of NZF (87.1 m^2/g) as compared with NZO (11.4 m^2/g) is the possible explanation of the variation in workability of AAS-NZF and AAS-NZO sets [48–50].

Measuring the initial and final setting times (IST and FST, respectively) is considered as one of the essential physical parameter that must be determined for AAS, to evaluate its availability in concrete making. As clarified in Fig. 8a, the addition of NZO has a strong impact on the elongation of both IST and FST, highlighting the retardation effect of this nano-oxide on the rate of AAS-activation process. At high pH, ZnO can interact with OH$^-$ of the alkaline medium to yield amorphous Zn(OH)$_2$ sheets. The later
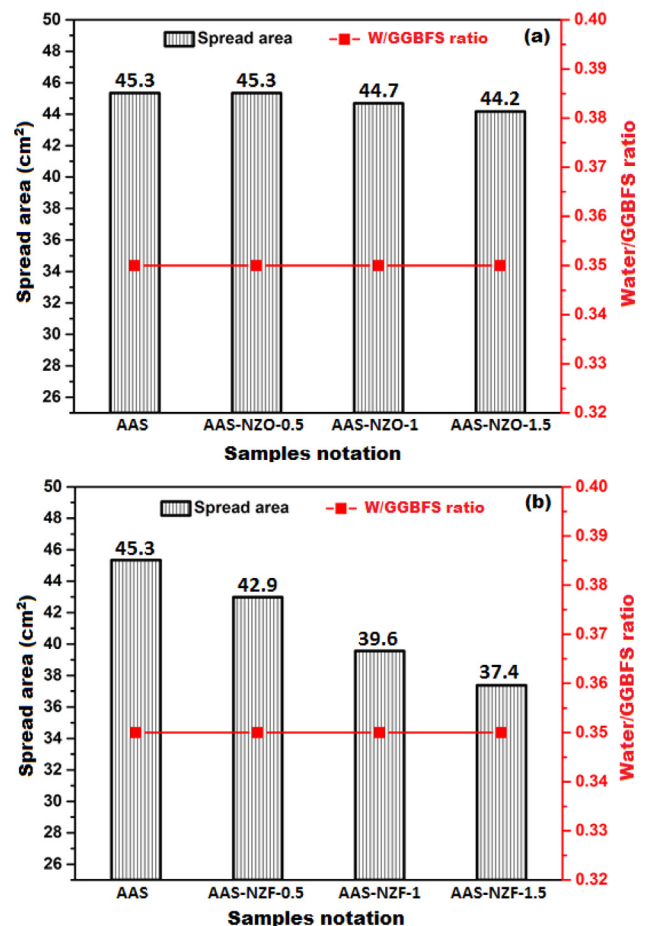

Fig. 7. Impact of different doses additions of (a) NZO and (b) NZF on the workability of AAS at constant Water/GGBFS ratio.
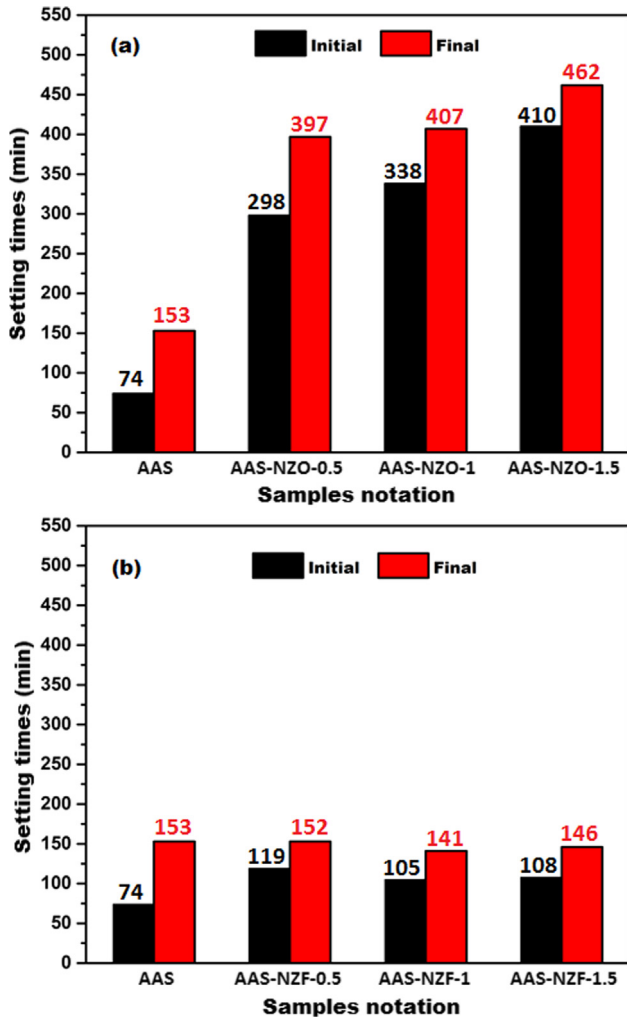
Fig. 8. Effect of different doses additions of (a) NZO and (b) NZF on the initial and final setting times of AAS.

Fig. 9. Compressive strength values for AAS containing different doses of (a) NZO and (b) NZF at different curing times.

form barrier layers between GGBFS grains and NaOH [27,51], resulting in the retardation of both dissolution and condensation rates of alkali activation process. On the other hand, all AAS-NZF composites demonstrate setting times nearly close to those of the control sample, Fig. 8b. This should be explained by the acceleration effect of $Fe_2O_4^{2-}$ resulted from the ionization of NZF in alkaline media, which compensates the retardation effect caused by ZnO [33,52]. The acceleration effect is mainly originated from the fact that Fe has vacant orbitals in d-level, which make this transition metal to form a complex with the activated species resulted from alkali-AAS activation.

The compressive strengths of hardened AAS, AAS-NZO and AAS-NZF composites at different hydration times up to 28-days are clarified in Fig. 9 (a, b). Generally, a gradual increase in compressive strength values was recorded with time advanced at all hardened mixtures. This gained trend is due to the continuation of slag dissolution/condensation with time of curing, resulting in a generation of successive binding-giving-phases contents. This is in line with recently published previous works [5,12,17,53,54]. The inclusion of NZO in NaOH-activated-GGBFS has a negative impact on its mechanical properties at 1 and 3 days of curing. This regression in compressive strength values increases with the increase of NZO addition level from 0.5% to 1.5%. An opposite trend was observed after 3 days of hydration as all hardened AAS-NZO demonstrate
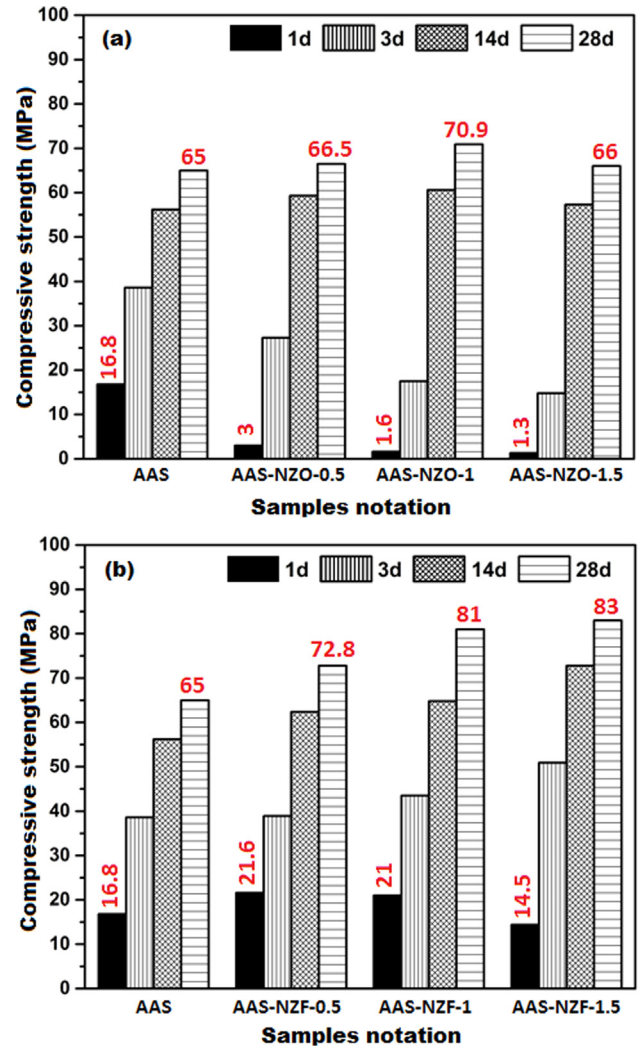
compressive strength values higher than those of reference sample (with no NZO). The possible explanation of these outcomes is the retardation property of NZO, which negatively affects the activation process of GGBFS at early curing times (1 and 3 days). In the alkaline pH value (higher than 12), NZO was converted into amorphous sheets of $Zn(OH)_2$ as it is regarded as a barrier layer to unreacted slag grains, leading to a temporary hindrance of slag activation. After 3 days of curing, the free Ca^{2+} ions (resulted from slag activation) interacts with $Zn(OH)_2$ to yield a crystalline calcium zincate hydrate phase (CZH: $CaZn_2(OH)_6.2\ H_2O$), which was detected by XRD and TGA/DTG techniques (See later Figs. 10-13). Once CZH is formed, the activation process of GGBFS starts again and extra amounts of binding products were generated [25,27,51]. Finally, all over of AAS-NZO composites, AAS pastes containing 1 wt% NZO possesses the highest strength, especially at 28 days of curing. Unlike AAS-NZO mixtures, the emending NZF-spinel in alkali activated system has resulted in a considerable compressive strength enhancement. Interestingly, There is no a retardation effect of Zn^{2+} in presence of $Fe_2O_4^{2-}$ ions (in AAS-NZF mixtures) so there is no strength deterioration in the early ages (1–3 days). The upgrade in the mechanical characteristics may be attributed to physical and chemical mechanisms. For physical mechanism, NZF-spinel as a whole acts as a specific motivator for slag activation process and works as nucleation centers for
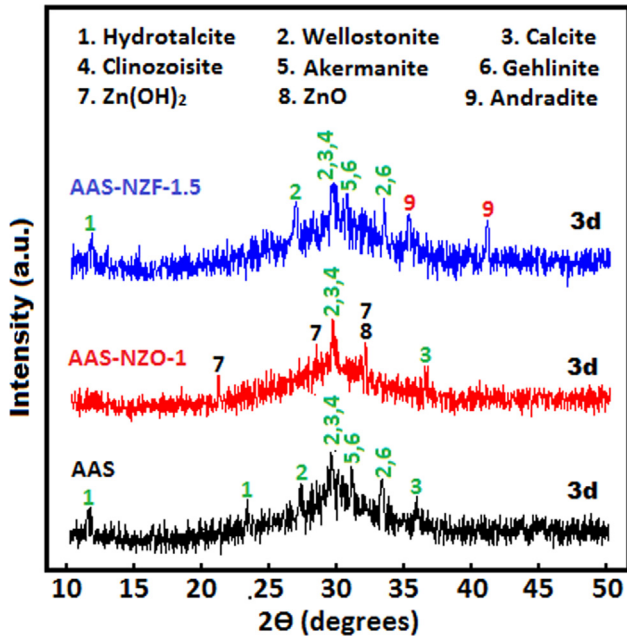
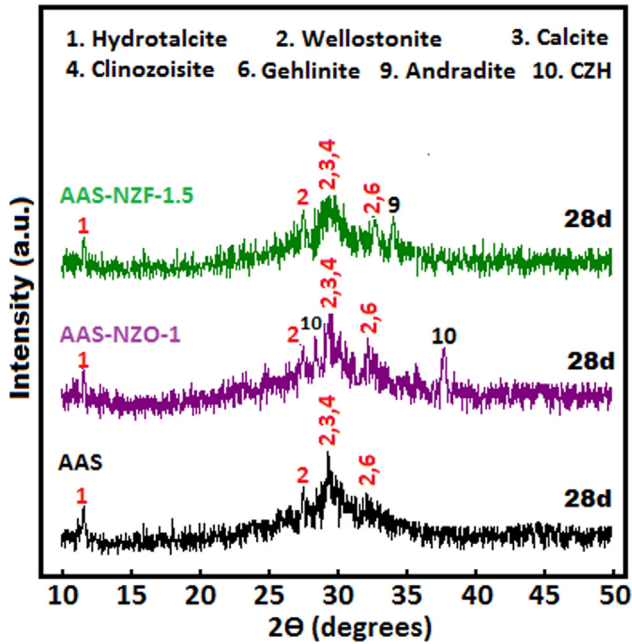**Fig. 10.** XRD-patterns for AAS, AAS-NZO-1 and AAS-NZF-1.5 at 3 days of curing.

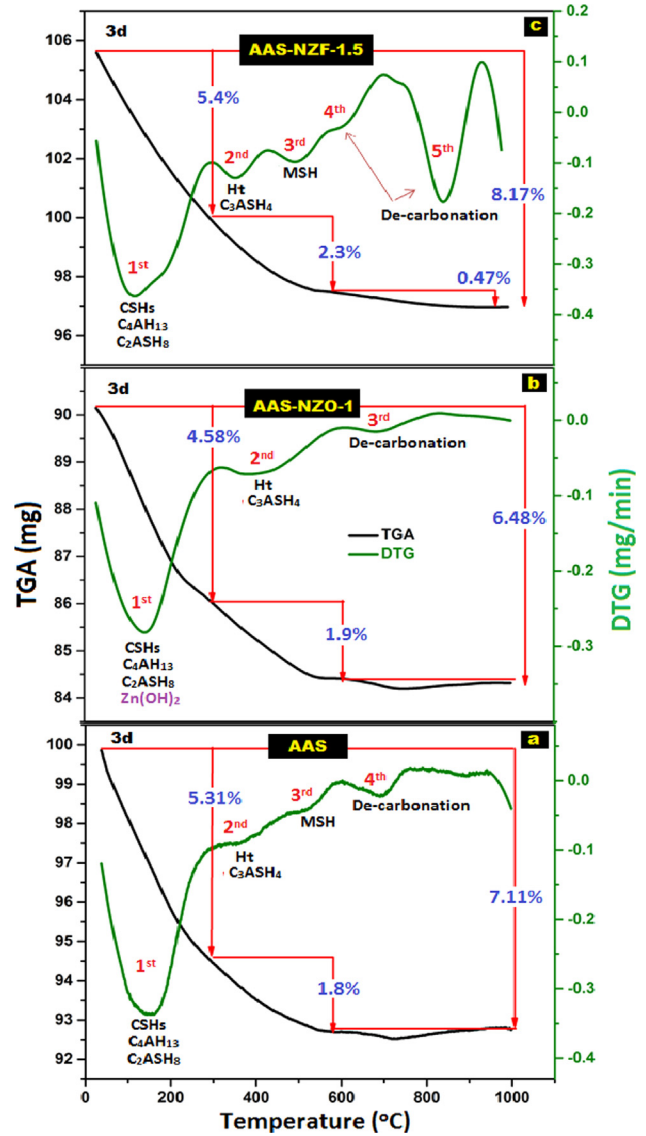**Fig. 11.** XRD-patterns for AAS, AAS-NZO-1 and AAS-NZF-1.5 at 28 days of curing.

Fig. 12. TGA/DTG curves for AAS, AAS-NZO-1 and AAS-NZF-1.5 at 3 days of curing.

hydration process to create extra amounts of binding phases. This perfectly highlights the enhancement of CSH, and CASH formation as identified by TG/DTG-analysis (See later Fig. 12). Meanwhile, the chemical mechanism can be represented as follows: in high alkaline media, NZF-spinel partially dissociates into Zn^{2+} and $Fe_2O_4^{2-}$ [33,52], the later can interact with free Ca^{2+} ions and SiO_2 to create supplemental hydration products like calcium ferrosilicate hydrate (CFSH). This is agreement with XRD-analysis (See F later Figs. 10, 11), which proved the formation of andradite phase ($Ca_3Fe_2(SiO_4)_3$) within alkali-activated composites. The hardened composites hav-

ing 0.5, 1.0, and 1.5 NZF-spinel were found to demonstrate 28-days compressive strength values 12, 25, and 28%, respectively, higher than that of reference mixture.

3.2. Phase identification

Fig. 10 displays XRD-patterns of AAS, AAS-NZO-1, and AAS-NZF-1.5 hydrated for 3-days. The patterns of all composites were found to exhibit a broad amorphous peak (located at 2θ range of 21–34°) which mainly affiliated to sodium aluminosilicate hydrate (N-A-S-H) [55,56]. Calcite and CSHs (as wollastonite and Clinozoisite phases) were observed at nearly 2θ of 29.32° [57]. The XRD-patterns of AAS and AAS-NZF-1.5 assigned to the formation of hydrotalcite phase, ($Mg_6Al_2(CO_3)(OH)_{16.4}$ (H_2O) which identified at 2θ of 11.7°. Although this phase is not determined in the case of AAS-NZO-1 sample, new peaks affiliated to $Zn(OH)_2$ were observed at 2θ of 20.9, 28.5 and 32.7° [27]. These outcomes proves the retardation of slag hydration which is mainly caused by the formation of $Zn(OH)_2$, negatively reflecting on the mechanical properties. Andradite phase ($Ca_3Fe_2Si_3O_{12}$) was observed at two different

Fig. 13. TGA/DTG curves for AAS, AAS-NZO-1 and AAS-NZF-1.5 at 28d days of curing.

bined water within the binding phases (C-S-H and CASH phases) was identified at temperature of 50–200 °C [2,60–65]. The weight loss appeared at 200–400 °C could be referred to the decomposition of Ht-phase and hydrogarnet (C_3ASH_4) [66–70]. Another weight loss identified at 500–600 °C may be due to the dehydration of magnesium silicate hydrate (MSH) [17,70]. The decomposition of carbonate-containing-phases (mainly calcium carbonate) has resulted in the appearance of CO_2-weight loss at 600–800 [71–74]. At the same curing age, the incorporation of 1 wt% NZO in alkali activated system (Fig. 12b) leads to a noticeable decrease in weight loss related to strength-giving-phases (CSH and CASH), confirming the retardation effect of NZO on the activation of slag hydration at early age of curing. An opposite trend was recorded in the case of AAS-NZF-1.5 curve as a considerable increase in the formation of CSH and CASH has been observed. These outcomes confirm the fact that NZF represents higher efficacy on the acceleration of activation process as compared with NZO, especially at early ages of curing (Fig. 12c).

The increase in curing time up to 28-days (Fig. 13 a-c) results in the same weight losses, but with higher values compared to that detected in 3-days-activated-samples. The increase in weight losses of hydration products confirms the alkali-activation process continuation with time advanced. Comparing with AAS, AAS-NZO-1 and AAS-NZF-1.5 were found to demonstrate higher 28-days weight losses. This proves the positive role of the prepared nanomaterials in the enhancement of AAS performance, reflecting on mechanical properties improvement.
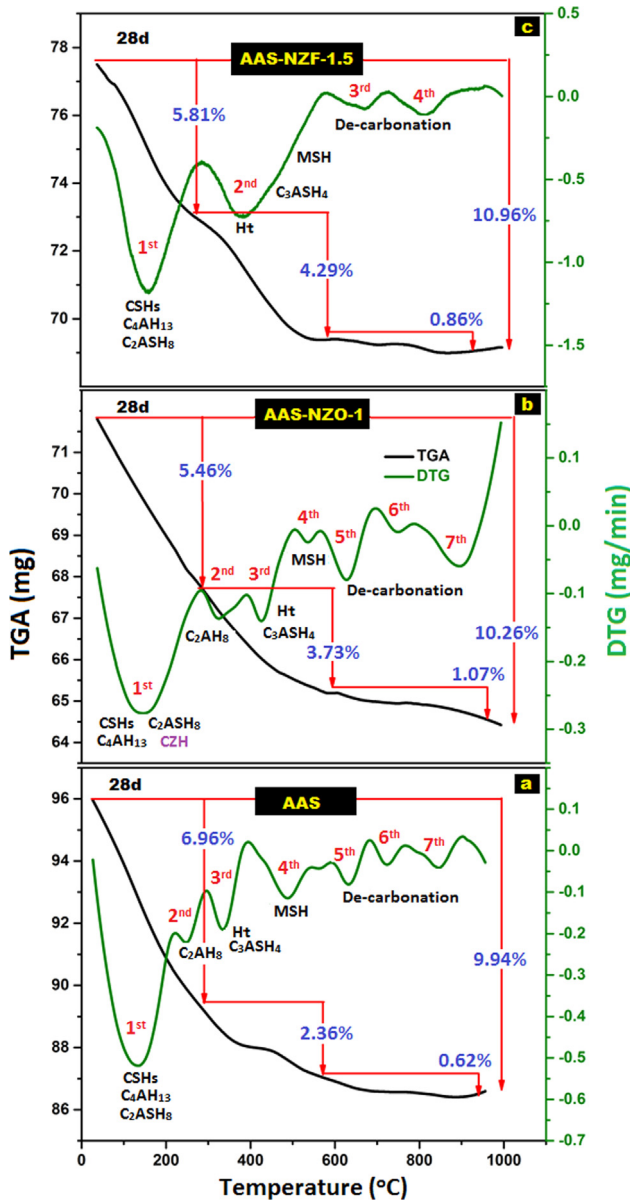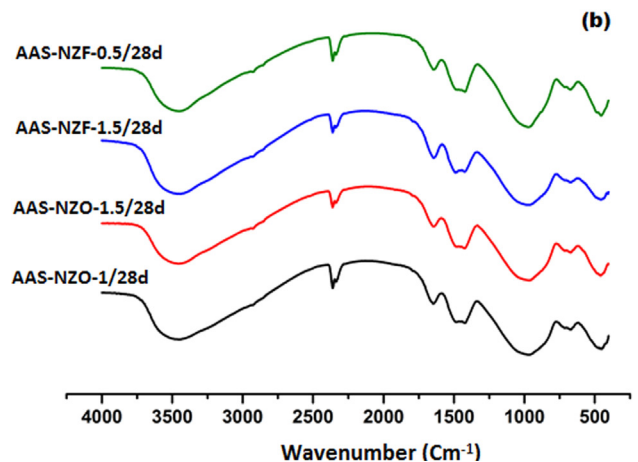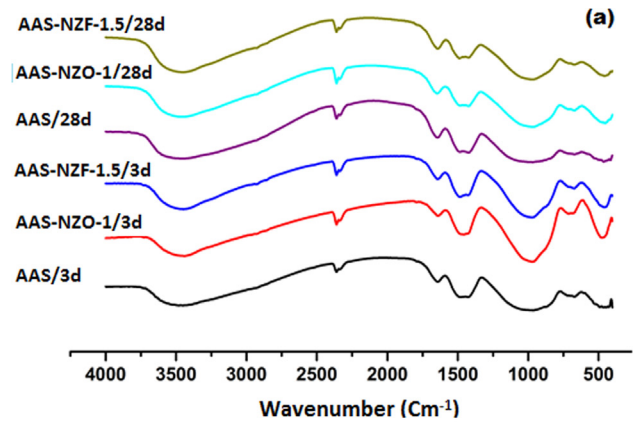

Fig. 14. FTIR-spectra for AAS, AAS-NZO and AAS-NZF at different ages of curing.

locations (2θ of 34.9 and 40.8°) [52,58] in the case of AAS-NZF-1.5 mixture. This is mainly originated from the interaction between ferrite ions and calcium silicate species to build CFSH (Andradite phase). With time advanced (up to 28-days), the most phases mentioned previously were identified, Fig. 11. Nevertheless, in the case of AAS-ZNO-1, the appearance of new peaks (at 2θ of 29 and 37.6°) affiliated to calcium zincate hydrate (CZH) [59] accompanied by the disappearance of $Zn(OH)_2$ gives a strong evidence on the acceleration of slag activation at later age of hydration (28 days).

Fig. 12 (a-c) demonstrates the TGA/DTG curves of AAS, AAS-NZO-1, and AAS-NZF-1.5 mixtures hydrated for 3-days. Generally, the increase in weight loss (calculated by TGA) directly reflects on the increase in the hydration products resulted from alkali activation process. For AAS, four weight losses (Fig. 12a) were detected at different temperature ranges. The weight loss characteristics for the dehydration of free, physically adsorbed, and chemically com-

The FTIR-spectra of 3- and 28-days hydrated AAS individually containing 1% NZO and 1.5% NZF, respectively, are depicts in Fig. 14a. Different transmittance bands have been detected at different wavenumbers (Table 4). At 3-days of curing, the incorporation of nano-oxides leads to the enhancement of O-Si-O band intensity. This could be due to the overlapping between O-Si-O and octahedral Zn-O [75,76] and Fe-O [77]. The intensity of this band remarkably decreases with the increase of curing time up to 28-days. The possible explanation of this observation is the interaction of Zn-O and Fe-O with Ca^{2+} (resulted from slag activation), producing CZH and CFSH-binding phases as previously proved by XRD-analysis (Figs. 10, 11). This outcome also proves the reason behind the positive impact of these nano-sized materials on the enhancement of mechanical properties with time. The increase of NZO and NZF contents causes a significant increase in the intensity of transmittance band appeared around 467 cm^{-1} (Fig. 14b). This should be explained by the fact that the dissolved Ca^{2+} from slag activation interacts with definite concentration of Zn-O and Fe-O. Other unreacted oxides could be maintained in pore structure of the alkali activated matrix, leading to the increase of this peak intensity.

Table 4
. Some important transmittance bands at different wavenumbers.

Wavenumber (cm^{-1})	Type of vibrational band
440–530	bending Si-O-Si, stretching Fe-O and Zn-O
698	symmetric stretching Si-O-Al
995	asymmetric stretching Si-O-Si(Al)
1460	symmetric stretching CO_3^{2-}
1640	bending H-O–H
2350	symmetric stretching O = C = O
3200–3600	symmetric stretching

3.3. Microstructure

The FE-SEM-photographs provided by EDS-analyses of AAS, AAS-NZO-1.0, and AAS-NZF-1.50 at 3 and 28-days of curing are depicted in Fig. 15. At all hardened samples, the enhancement in hydration products formation accompanied by microstructure compaction is an indication of the continuation of slag hydration with curing time, agreeing with the previous published works [17,57]. A low compact microstructure with the appearance of spherical-shaped $Zn(OH)_2$ layer on slag particles is the mean feature of 3 days-AAS-NZO-1.0 microstructure. This is in line with compressive strength results, which proved that the negative effect of NZO on the binding capacity of AAS at 3-days of curing. After 28-days of hydration, this layer disappears and centers of CZH phase (as proved by EDS) were distributed along microstructure. This confirms the results of XRD-analysis of AAS-NZO mixtures as CZH-phase was clearly identified at 28-days of curing. The AAS-NZF-1.50 mixture seems to exhibit microstructure compaction better than those of AAS, AAS-NZO-1.0 at both 3- and 28-days. This perfectly highlights the acceleration effect of NZF on the activation process, leading to the excessive formation of strength-giving-phases (CSH, CASH, and CFSH). The FE-SEM/EDS analyses of all activated samples are in a good harmony with XRD-, and TG/DTG-results.

3.4. Radiation shielding

The variations in the mitigation of harmful γ-ray radiation depend on various factors such as the operating temperature [33], the type of additives and the pore structure [29,34]. The porosity and compressive strength play a circular role in the enhancement of the hardened alkali-activated materials feasibility in γ radiation shielding. As shown in Fig. 16 (a, b), the increase in compressive strength of the hardened materials reflects on a
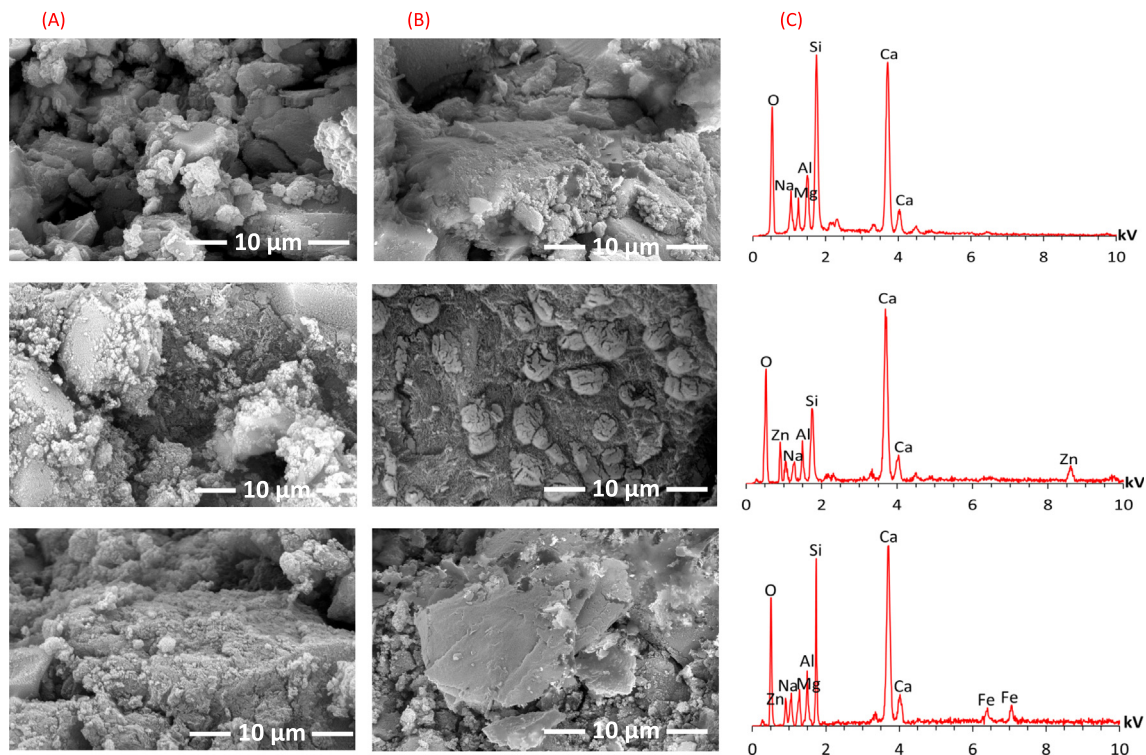

Fig. 15. FESEM-photographs of AAS, AAS-NZO-1.0, and AAS-NZF-1.5 mixtures (from top to bottom) at (A) 3- and (B) 28-days provided by (C) EDS-analyses.
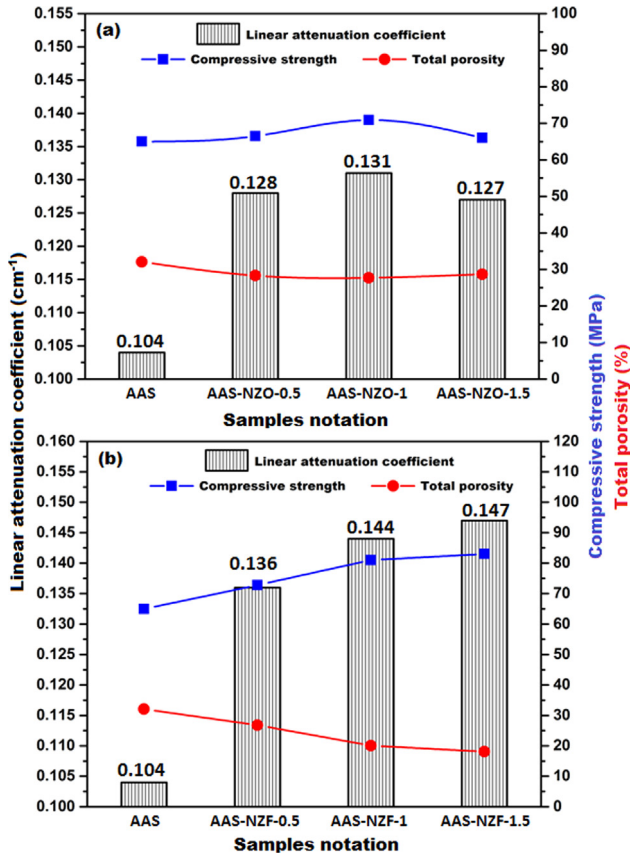
Fig. 16. Relationship between 28-days compressive strength, total porosity and attenuation coefficient values for AAS containing different contents of (a) NZO and (b) NZF.
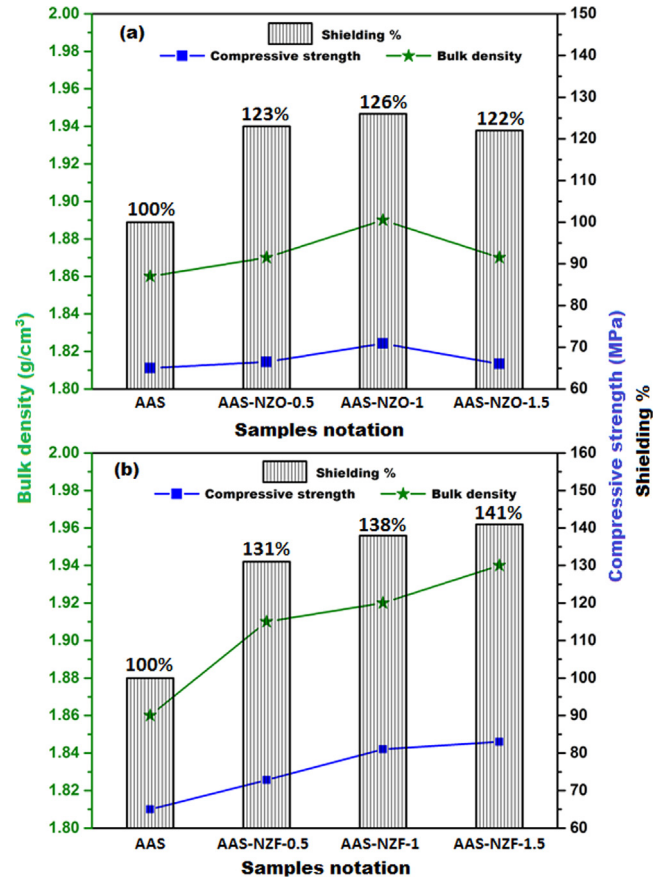

Fig. 17. Relationship between 28-days compressive strength, bulk density and shielding % for AAS containing different contents of (a) NZO and (b) NZF.

significant reduction in total porosity accompanied by high γ-ray radiation shielding values. Accordingly, reverse relationships between strength and total porosity as well as radiation shielding and total porosity have been recorded. In the same direction, the compressive strength and bulk density are two key points which result in an increment in linear attenuation coefficient value, Fig. 17 (a, b). The alkali-activated system with high compressive strength demonstrates high bulk density and high linear attenuation coefficient values. Regardless the higher capability of AAS-NZF samples in radiation shielding compared to AAS-NZO set, desirable NZO and NZF contents (1 and 1.5 wt%, respectively) causes the improvement in the physical and mechanical properties of AAS. This is mainly originated from the fact that the formation of new strength-giving-phases (CZH and CSFH) [28,29] which precipitate in open pores, leading to a remarkable reduction in total porosity accompanied by a considerable increment in bulk density of the hardened activated materials. The positive impact of desirable nano-oxides content on the physical and mechanical performances of the hardened alkali-activated materials has reflected on their effectiveness in γ-ray radiation shielding. On the other hand, the type of additive also plays a vital role in the shielding property. According our study, the attenuation coefficient values for AAS-ZnFe$_2$O$_4$ are higher as compared with attenuation coefficient values of AAS-ZnO. This finding also is attributed to that ZnFe$_2$O$_4$ considered spinel ferrite of specific crystallographic structure [30,31] geometry $[Zn^{2+}]_{tetrahedral}[Fe_2O_4^2]_{octahedral}$ and acts as dosimetric material with high absorption power for harmful radiations [32]. All of these outcomes are fully consistent with some of recent publications in which the attenuation coefficient value at room temperature for some cementitious composites increased by 11% in presence of Fe$_2$O$_3$ but in

presence of spinel ferrites, the values reached to 26–32%. [29,33,34].

3.5. Anti-fungal activity

The deterioration effects of some organisms on concrete properties including strength regression and steel corrosion is the reasonable reason behind conducting this testing on some selected samples containing nano-materials. The harmful effect of microorganisms is mainly originated from the formation of biomass on concrete surface accompanied by the creation of acidic media, which results in a degradation in the binding capacity of concrete, notably the induction of steel corrosion [15]. Fig. 18 shows the digital photos of fungal cultures containing nano-modified AAS discs. The growth grades {based on visual observations according to ASTM D4300-1, (2013) [44] of three fungal strains in each case are reported in Table 5. Generally, the incorporation of nano-materials in alkali activated system was found to have a significant effect on fungal growth inhibition at all applied strains. Nevertheless, nano-modified AAS samples demonstrate inhibition rate in the case of *Aspergillus niger* higher than those of observed in *Aspergillus fumigatus* and *Aspergillus terreus* strains. Same results have been achieved by Abdel-Gawwad et al.[17] in alkali activated system having Pb-rich-sludge. Comparing with AAS-NZO-1.5, AAS sample having 1.5 wt% NZF represents the higher impact on fungal growth inhibition through all strains. This indicates that the promising physical and mechanical properties of AAS-NZF samples is not only the main reason behind its preferable use in construction projects, but also its high resistivity against detrimental fungal strains make it is beneficially applied in locations rich with microorganisms, especially in sewer system.
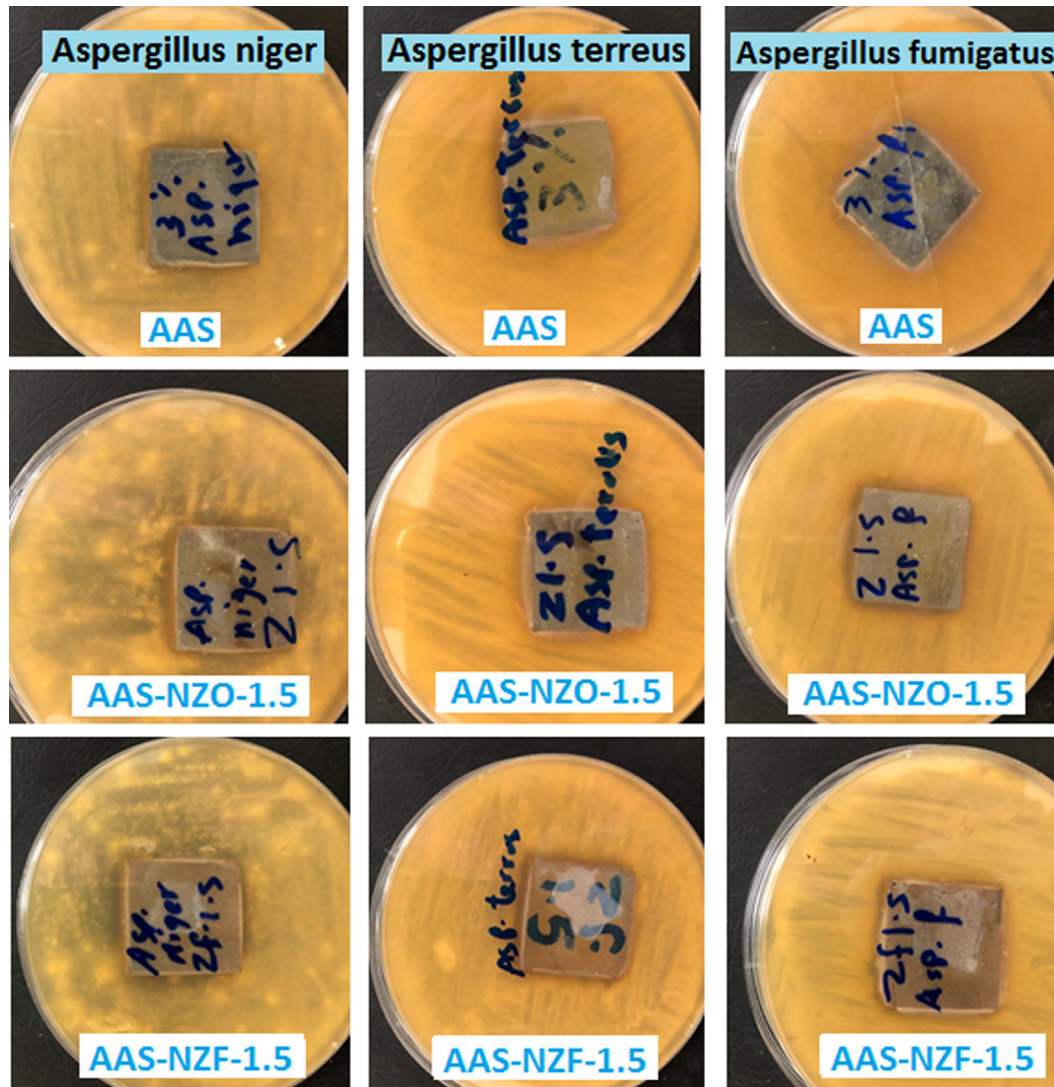
Fig. 18. Digital photos for different types of fungal cultures containing AAS discs with and without NPs.

Table 5
. Growth grad of fungal agar media containing different hardened samples (HG: high growth; MG: moderate growth; LG: light growth; SG: spare growth).

Sample notations	Fungal growth grade (ASTM D4300-1, (2013)		
	Aspergillus fumigatus	Aspergillus niger	Aspergillus terreus
AAS	HG	MG	HG
AAS-NZO-1.5	MG	LG	MG
AAS-NZF-1.5	MG	SG	MG

4. Conclusions

The individual impact of nano-zinc oxide and -zinc ferrite on the physical and mechanical properties of alkali activated slag at both early and later ages has been addressed. Low sodium hydroxide content (3 wt%) was used in the activation process to optimize the cost and to mitigate the CO_2-emission caused by alkali-activated materials manufacturing. Several findings can be concluded as follows:

- The addition of zinc oxide was found to have a negative impact on the physical and mechanical properties of alkali activated slag cement. The retardation effect is mainly resulted from the formation of barrier layers of zinc hydroxide on slag grains.
- The inhibitory effect of nano-zinc oxide diminished with time advanced, since zinc hydroxide did interact with the dissolved calcium to yield calcium zincate hydrate binding phase as proved by x-ray diffraction analysis.
- Nano-zinc ferrite showed an acceleration effect on the hydration rate of alkali activated slag performance at all curing ages as confirmed by compressive strength testing. Additionally, the addition of 1.5 nano-zinc ferrite has resulted in the highest improvement in the performance of hardened alkali-activated material comprising the highest bulk density (1.95) and compressive strength (83 MPa) accompanied by the lowest total porosity (18%) at 28-days of curing. This positively reflected on the formation of alkali activated material with high compaction which can be beneficially used in γ-ray radiation shielding.
- An observable fungal growth inhibition rate was recorded when nano-modified alkali activated slag mixtures were exposed to detrimental two-fungal species, suggesting the application feasibility of this cement in locations rich with harmful microorganisms.

CRediT authorship contribution statement

Alaa Mohsen: Writing - original draft, Formal analysis, Data curation. **Hamdy A. Abdel-Gawwad:** Writing - original draft, Formal analysis, Data curation. **M. Ramadan:** Writing - original draft, Formal analysis, Data curation.

Declaration of Competing Interest

The authors declare that they have no known competing financial interests or personal relationships that could have appeared to influence the work reported in this paper.

References

[1] H. Abdel-Gawwad, S.A. El-Aleem, A. Amer, H. El-Didamony, M. Arif, Combined impact of silicate-amorphicity and MgO-reactivity on the performance of Mg-silicate cement, Constr. Build. Mater. 189 (2018) 78–85.

[2] H. Abdel-Gawwad, K.A. Khalil, Application of thermal treatment on cement kiln dust and feldspar to create one-part geopolymer cement, Constr. Build. Mater. 187 (2018) 231–237.

[3] P. Awoyera, A. Adesina, A critical review on application of alkali activated slag as a sustainable composite binder, Case Stud. Constr. Mater. 11 (2019) e00268.

[4] M. Jiang, X. Chen, F. Rajabipour, C.T. Hendrickson, Comparative life cycle assessment of conventional, glass powder, and alkali-activated slag concrete and mortar, J. Infrastruct. Syst. 20 (4) (2014) 04014020.

[5] B. Vafaei, K. Farzanian, A. Ghahremaninezhad, The influence of superabsorbent polymer on the properties of alkali-activated slag pastes, Constr. Build. Mater. 236 (2020) 117525.

[6] A. Purdon, The action of alkalis on blast-furnace slag, J. Soc. Chem. Ind. 59 (9) (1940) 191–202.

[7] F. Collins, J.G. Sanjayan, Effect of pore size distribution on drying shrinking of alkali-activated slag concrete, Cem. Concr. Res. 30 (9) (2000) 1401–1406.

[8] F. Puertas, B. González-Fonteboa, I. González-Taboada, M. Alonso, M. Torres-Carrasco, G. Rojo, F. Martínez-Abella, Alkali-activated slag concrete: Fresh and hardened behaviour, Cem. Concr. Compos. 85 (2018) 22–31.

[9] F. Puertas, C. Varga, M. Alonso, Rheology of alkali-activated slag pastes Effect of the nature and concentration of the activating solution, Cement Concr. Compos. 53 (2014) 279–288.

[10] W.-J. Long, B.-X. Xiao, Y.-C. Gu, F. Xing, Micro-and macro-scale characterization of nano-SiO2 reinforced alkali activated slag composites, Mater. Charact. 136 (2018) 111–121.

[11] K. Behfarnia, M. Rostami, Effects of micro and nanoparticles of SiO2 on the permeability of alkali activated slag concrete, Constr. Build. Mater. 131 (2017) 205–213.

[12] H.A. Abdel-Gawwad, M.S. Mohammed, T. Alomayri, Single and dual effects of magnesia and alumina nano-particles on strength and drying shrinkage of alkali activated slag, Constr. Build. Mater. 228 (2019) 116827.

[13] A. Nazari, S. Riahi, The effects of ZnO2 nanoparticles on properties of concrete using ground granulated blast furnace slag as binder, Mater. Res. 14 (3) (2011) 299–306.

[14] M. Sarkar, M. Maiti, S. Maiti, S. Xu, Q. Li, ZnO-SiO2 nanohybrid decorated sustainable geopolymer retaining anti-biodeterioration activity with improved durability, Mater. Sci. Eng., C 92 (2018) 663–672.

[15] H. Abdel-Gawwad, S.A. El-Aleem, S.A. El-Enein, M. Khalifa, Resistivity of eco-friendly alkali activated industrial solid wastes against sulfur oxidizing bacteria, Ecol. Eng. 112 (2018) 1–9.

[16] D.H. Nies, Microbial heavy-metal resistance, Appl. Microbiol. Biotechnol. 51 (6) (1999) 730–750.

[17] H.A. Abdel-Gawwad, S.A. Mohamed, M.S. Mohammed, Recycling of slag and lead-bearing sludge in the cleaner production of alkali activated cement with high performance and microbial resistivity, J. Cleaner Prod. 220 (2019) 568–580.

[18] S. Inamdar, K. Rajpure, High-performance metal–semiconductor–metal UV photodetector based on spray deposited ZnO thin films, J. Alloy. Compd. 595 (2014) 55–59.

[19] F. Pacheco-Torgal, S. Jalali, Nanotechnology: advantages and drawbacks in the field of construction and building materials, Constr. Build. Mater. 25 (2) (2011) 582–590.

[20] Y. Liu, Z. Lin, W. Lin, K.S. Moon, C. Wong, Reversible superhydrophobic–superhydrophilic transition of ZnO nanorod/epoxy composite films, ACS Appl. Mater. Interfaces 4 (8) (2012) 3959–3964.

[21] L. Zhang, Y. Jiang, Y. Ding, M. Povey, D. York, Investigation into the antibacterial behaviour of suspensions of ZnO nanoparticles (ZnO nanofluids), J. Nanopart. Res. 9 (3) (2007) 479–489.

[22] V. Singh, K. Sandeep, H. Kushwaha, S. Powar, R. Vaish, Photocatalytic, hydrophobic and antimicrobial characteristics of ZnO nano needle embedded cement composites, Constr. Build. Mater. 158 (2018) 285–294.

[23] T. Noeiaghaei, N. Dhami, A. Mukherjee, Nanoparticles surface treatment on cemented materials for inhibition of bacterial growth, Constr. Build. Mater. 150 (2017) 880–891.

[24] M. Li, S. Deng, Y. Yu, J. Jin, Y. Yang, X. Guo, Mechanical properties and microstructure of oil well cement stone enhanced with Tetra-needle like ZnO whiskers, Constr. Build. Mater. 135 (2017) 59–67.

[25] F.F. Ataie, M.C. Juenger, S.C. Taylor-Lange, K.A. Riding, Comparison of the retarding mechanisms of zinc oxide and sucrose on cement hydration and interactions with supplementary cementitious materials, Cem. Concr. Res. 72 (2015) 128–136.

[26] T. Nochaiya, Y. Sekine, S. Choopun, A. Chaipanich, Microstructure, characterizations, functionality and compressive strength of cement-based materials using zinc oxide nanoparticles as an additive, J. Alloy. Compd. 630 (2015) 1–10.

[27] X. Cong, W. Zhou, X. Geng, M. Elchalakani, Low field NMR relaxation as a probe to study the effect of activators and retarders on the alkali-activated GGBFS setting process, Cem. Concr. Compos. 104 (2019) 103399.

[28] I. Akkurt, H. Akyildirim, B. Mavi, S. Kilincarslan, C. Basyigit, Gamma-ray shielding properties of concrete including barite at different energies, Prog. Nucl. Energy 52 (7) (2010) 620–623.

[29] S. Abo-El-Enein, F. El-Hosiny, S. El-Gamal, M. Amin, M. Ramadan, Gamma radiation shielding, fire resistance and physicochemical characteristics of Portland cement pastes modified with synthesized Fe2O3 and ZnO nanoparticles, Constr. Build. Mater. 173 (2018) 687–706.

[30] J. Wrzyszcz, M. Zawadzki, A.M. Trzeciak, J.J. Ziółkowski, Rhodium complexes supported on zinc aluminate spinel as catalysts for hydroformylation and hydrogenation: preparation and activity, J. Mol. Catal. A: Chem. 189 (2) (2002) 203–210.

[31] R. Raveendra, P. Prashanth, B. Daruka Prasad, S. Chandra Nayaka, G. Suresha, B. Nagabhushana, H. Nagabhushana, N. Bhagya, Synthesis, characterization and antibacterial activity of zinc ferrite nanopowder, Int. J. Sci. Res. 1(4) (2013)

[32] S. Raut, V. Awasarmol, S. Shaikh, B. Ghule, S. Ekar, R. Mane, P. Pawar, Study of gamma ray energy absorption and exposure buildup factors for ferrites by geometric progression fitting method, Radiat Eff. Defects Solids 173 (3–4) (2018) 329–338.

[33] M. Ramadan, M. Amin, M.A. Sayed, Superior physico-mechanical, fire resistivity, morphological characteristics and gamma radiation shielding of hardened OPC pastes incorporating ZnFe2O4 spinel nanoparticles, Constr. Build. Mater. 234 (2020) 117807.

[34] M. Ramadan, S. El-Gamal, F. Selim, Mechanical properties, radiation mitigation and fire resistance of OPC-recycled glass powder composites containing nanoparticles, Constr. Build. Mater. 251 (2020) 118703.

[35] P. Suppuraj, G. Thirunarayanan, M. Swaminathan, I. Muthuvel, Facile synthesis of spinel nanocrystalline ZnFe2O4: enhanced photocatalytic and microbial applications, Mater. Sci. Appl. Chem. 34 (1) (2017) 5–11.

[36] X. Zhao, F. Lou, M. Li, X. Lou, Z. Li, J. Zhou, Sol– gel-based hydrothermal method for the synthesis of 3D flower-like ZnO microstructures composed of nanosheets for photocatalytic applications, Ceram. Int. 40 (4) (2014) 5507–5514.

[37] Y.-X. Wang, J. Sun, X. Fan, X. Yu, A CTAB-assisted hydrothermal and solvothermal synthesis of ZnO nanopowders, Ceram. Int. 37 (8) (2011) 3431–3436.

[38] M. Qin, Q. Shuai, G. Wu, B. Zheng, Z. Wang, H. Wu, Zinc ferrite composite material with controllable morphology and its applications, Mater. Sci. Eng., B 224 (2017) 125–138.

[39] R. Rahimi, H. Kerdari, M. Rabbani, M. Shafiee, Synthesis, characterization and adsorbing properties of hollow Zn-Fe2O4 nanospheres on removal of Congo red from aqueous solution, Desalination 280 (1–3) (2011) 412–418.

[40] S.M. Hoque, M.S. Hossain, S. Choudhury, S. Akhter, F. Hyder, Synthesis and characterization of ZnFe2O4 nanoparticles and its biomedical applications, Mater. Lett. 162 (2016) 60–63.

[41] ASTM C1611, Standard test method for slump flow of self-consolidating concrete, (2009).

[42] A. Habib, I. Aiad, T. Youssef, A.A. El-Aziz, Effect of some chemical admixtures on the physico-chemical and rheological properties of oil well cement pastes, Constr. Build. Mater. 120 (2016) 80–88.

[43] A. Designation, C191: Standard test method for normal consistency and setting time of Hydraulic Cement ", Annual Book of ASTM Standards (2008) 172-174.

[44] ASTM C109M, Standard test method for compressive strength of hydraulic cement mortars (using 2-in. or [50-mm] cube specimens), Annual Book of ASTM StandardsAnnual Book of ASTM Standards 4(1) (2013) 1-9.

[45] ASTM C140, Standard test methods for sampling and testing concrete masonry units and related units, (2008).

[46] C.P. McHugh, P. Zhang, S. Michalek, P.D. Eleazer, pH required to kill Enterococcus faecalis in vitro, J. Endodontics 30 (4) (2004) 218–219.

[47] H.A. Abdel-Gawwad, M.S. Mohammed, M. Heikal, Ultra-lightweight porous materials fabrication and hazardous lead-stabilization through alkali-activation/sintering of different industrial solid wastes, J. Cleaner Prod. 244 (2020) 118742.

[48] J. Liu, H. Jin, C. Gu, Y. Yang, Effects of zinc oxide nanoparticles on early-age hydration and the mechanical properties of cement paste, Constr. Build. Mater. 217 (2019) 352–362.

[49] X. Gao, Q. Yu, H. Brouwers, Characterization of alkali activated slag–fly ash blends containing nano-silica, Constr. Build. Mater. 98 (2015) 397–406.

[50] M. Heikal, H.A. Abdel-Gawwad, F.A. Ababneh, Positive impact performance of hybrid effect of nano-clay and silica nano-particles on composite cements, Constr. Build. Mater. 190 (2018) 508–516.

[51] N. Garg, C.E. White, Mechanism of zinc oxide retardation in alkali-activated materials: an in situ X-ray pair distribution function investigation, J. Mater. Chem. A 5 (23) (2017) 11794–11804.

[52] C. Zhang, L. Zhuang, J. Wang, J. Bai, W. Yuan, Extraction of zinc from zinc ferrites by alkaline leaching: enhancing recovery by mechanochemical reduction with metallic iron, J. South Afr. Inst. Min. Metall. 116 (12) (2016) 1111–1114.

[53] H.A. Abdel-Gawwad, A.M. Rashad, M. Heikal, Sustainable utilization of pretreated concrete waste in the production of one-part alkali-activated cement, J. Cleaner Prod. (2019).

[54] N.T. Abdel-Ghani, H.A. Elsayed, S. AbdelMoied, Geopolymer synthesis by the alkali-activation of blastfurnace steel slag and its fire-resistance, HBRC J. 14 (2) (2018) 159–164.

[55] M. Heikal, M. Nassar, G. El-Sayed, S. Ibrahim, Physico-chemical, mechanical, microstructure and durability characteristics of alkali activated Egyptian slag, Constr. Build. Mater. 69 (2014) 60–72.

[56] S.-D. Wang, K.L. Scrivener, Hydration products of alkali activated slag cement, Cem. Concr. Res. 25 (3) (1995) 561–571.

[57] F.A. Ababneh, A.I. Alakhras, M. Heikal, S.M. Ibrahim, Stabilization of lead bearing sludge by utilization in fly ash-slag based geopolymer, Constr. Build. Mater. 227 (2019) 116694.

[58] A. Wang, H. Liu, X. Hao, Y. Wang, X. Liu, Z. Li, Geopolymer Synthesis Using Garnet Tailings from Molybdenum Mines, Minerals 9 (1) (2019) 48.

[59] X. Zhu, H. Yang, X. Ai, J. Yu, Y. Cao, Structural and electrochemical characterization of mechanochemically synthesized calcium zincate as rechargeable anodic materials, J. Appl. Electrochem. 33 (7) (2003) 607–612.

[60] H. Abdel-Gawwad, M. Heikal, M.S. Mohammed, S.A. El-Aleem, H.S. Hassan, S.V. García, A.M. Rashad, Evaluating the impact of nano-magnesium calcite waste on the performance of cement mortar in normal and sulfate-rich media, Constr. Build. Mater. 203 (2019) 392–400.

[61] H. Abdel-Gawwad, S.V. García, H.S. Hassan, Thermal activation of air cooled slag to create one-part alkali activated cement, Ceram. Int. 44 (12) (2018) 14935–14939.

[62] H. Abdel-Gawwad, E. Heikal, H. El-Didamony, F. Hashim, A.H. Mohammed, Recycling of concrete waste to produce ready-mix alkali activated cement, Ceram. Int. 44 (6) (2018) 7300–7304.

[63] H. El-Didamony, A.I. Hafez, M.S. Mohammed, R. Sabry, Prepared and properties of filled and pozzolanic-filled cements from marble dust waste and granulated slag, Journal of Thermal Analysis and Calorimetry 1-9.

[64] H.A. Abdel-Gawwad, M. Heikal, M.S. Mohammed, S.A. El-Aleem, H.S. Hassan, S. V. García, T. Alomayri, Sustainable disposal of cement kiln dust in the production of cementitious materials, J. Cleaner Prod. (2019).

[65] S. El-Gamal, S. Abo-El-Enein, F. El-Hosiny, M. Amin, M. Ramadan, Thermal resistance, microstructure and mechanical properties of type I Portland cement pastes containing low-cost nanoparticles, J. Therm. Anal. Calorim. 131 (2) (2018) 949–968.

[66] S. El-Gamal, F. El-Hosiny, M. Amin, D. Sayed, Ceramic waste as an efficient material for enhancing the fire resistance and mechanical properties of hardened Portland cement pastes, Constr. Build. Mater. 154 (2017) 1062–1078.

[67] M.B. Haha, B. Lothenbach, G. Le Saout, F. Winnefeld, Influence of slag chemistry on the hydration of alkali-activated blast-furnace slag—Part I: Effect of MgO, Cem. Concr. Res. 41 (9) (2011) 955–963.

[68] M.B. Haha, B. Lothenbach, G. Le Saout, F. Winnefeld, Influence of slag chemistry on the hydration of alkali-activated blast-furnace slag—Part II: Effect of Al2O3, Cem. Concr. Res. 42 (1) (2012) 74–83.

[69] F. Jin, K. Gu, A. Al-Tabbaa, Strength and hydration properties of reactive MgO-activated ground granulated blastfurnace slag paste, Cem. Concr. Compos. 57 (2015) 8–16.

[70] H. Abdel-Gawwad, S.A. El-Aleem, Effect of reactive magnesium oxide on properties of alkali activated slag geopolymer cement pastes, Ceramics-Silikáty 59 (1) (2015) 37–47.

[71] H. Abdel-Gawwad, S.A. El-Enein, M. Heikal, S.A. El-Aleem, A. Amer, I. El-Kattan, Synergistic effects of curing conditions and magnesium oxide addition on the physico-mechanical properties and firing resistivity of Portland cement mortar, Constr. Build. Mater. 176 (2018) 676–689.

[72] S. Abo-El-Eanein, H. Abdel-Gawwad, A.M. El-Mesallamy, H.I. El-Belbasi, H.G. Ayoub, Mechanical properties and microstructure of innovative bio-mortar containing different aggregates, Geosyst. Eng. 21 (5) (2018) 291–296.

[73] H. Abdel-Gawwad, Performance of bio-mortar under elevated temperatures, J. Therm. Anal. Calorim. 130 (3) (2017) 1439–1444.

[74] H.A. Gawwad, S.A.E.-A. Mohamed, S.A. Mohammed, Impact of magnesium chloride on the mechanical properties of innovative bio-mortar, Mater. Lett. 178 (2016) 39–43.

[75] R. Wang, Z. Yang, B. Yang, X. Fan, T. Wang, A novel alcohol-thermal synthesis method of calcium zincates negative electrode materials for Ni–Zn secondary batteries, J. Power Sources 246 (2014) 313–321.

[76] M. Kamani, A. Yourdkhani, R. Poursalehi, R. Sarraf-Mamoory, Studying the cold sintering process of zinc ferrite as an incongruent dissolution system, Int. J. Ceram. Eng. Sci. 1 (3) (2019) 125–135.

[77] A. Hernández, L. Maya, E. Sánchez-Mora, E.M. Sánchez, Sol-gel synthesis, characterization and photocatalytic activity of mixed oxide ZnO-Fe 2 O 3, J. Sol-Gel Sci. Technol. 42 (1) (2007) 71–78.